PHILOSOPHICAL TRANSACTIONS
OF THE ROYAL SOCIETY A
MATHEMATICAL, PHYSICAL AND ENGINEERING SCIENCES

Thermal jet drilling of granite rock: a numerical 3D finite element study

Journal:	*Philosophical Transactions A*
Manuscript ID	RSTA-2020-0128.R1
Article Type:	Research
Date Submitted by the Author:	29-Jun-2020
Complete List of Authors:	Saksala, Timo; Tampere University - Hervanta Campus Kouhia, Reijo; Tampere University - Hervanta Campus Mardoukhi, Ahmad; Tampere University - Hervanta Campus Hokka, Mikko; Tampere University - Hervanta Campus
Issue Code (this should have already been entered and appear below the blue box, but please contact the Editorial Office if it is not present):	FDSM
Subject:	Civil engineering < ENGINEERING AND TECHNOLOGY, Engineering geology < ENGINEERING AND TECHNOLOGY
Keywords:	thermal spallation, thermal jet drilling, rock fracture, finite elements, material modelling

Author-supplied statements

Relevant information will appear here if provided.

Ethics

Does your article include research that required ethical approval or permits?:
This article does not present research with ethical considerations

Statement (if applicable):
CUST_IF_YES_ETHICS :No data available.

Data

It is a condition of publication that data, code and materials supporting your paper are made publicly available. Does your paper present new data?:
My paper has no data

Statement (if applicable):
CUST_IF_YES_DATA :No data available.

Conflict of interest

I/We declare we have no competing interests

Statement (if applicable):
CUST_STATE_CONFLICT :No data available.

Authors' contributions

This paper has multiple authors and our individual contributions were as below

Statement (if applicable):
TS conceived the idea of this work and performed the numerical analyses. TS also wrote the first draft of the paper. AM and MH performed the experimental work. RK contributed to the thermo-mechanical modelling issues. All authors contributed to the analysis of the results and the final form of the paper.

PHILOSOPHICAL TRANSACTIONS A

Phil. Trans. R. Soc. A.
doi:10.1098/not yet assigned

Thermal jet drilling of granite rock: a numerical 3D finite element study

Timo Saksala[1], Reijo Kouhia[1] Ahmad Mardoukhi[2] and Mikko Hokka[2]

[1]Civil Engineering, Tampere University, FI-33101, Tampere, Finland, Orcid: 0000-0002-6159-3458
[2]Engineering Materials Science, Tampere University, FI-33101, Tampere, Finland

Keywords: thermal spallation, thermal jet drilling, rock fracture, finite elements, material modelling

Summary

This paper presents a numerical study on thermal jet drilling of granite rock that is based on thermal spallation phenomenon. For this end, a numerical method based on finite elements and a damage-viscoplasticity model is developed for solving the underlying coupled thermo-mechanical problem. An explicit time stepping scheme is applied in solving the global problem, which in the present case is amenable to extreme mass scaling. Rock heterogeneity is accounted for as random clusters of finite elements representing rock constituent minerals. The numerical approach is validated based on experiments on thermal shock weakening effect of granite in dynamic Brazilian disc test. The validated model is applied in 3D simulations of thermal jet drilling with a short duration (0.2 s) and high intensity (~3 MW/m^2) thermal flux. The present numerical approach predicts the spalling as a highly (tensile) damaged rock. Finally, it shown that thermal drilling exploiting heating-forced cooling cycles is a viable method when drilling in hot rock mass.

Introduction

Traditionally, drilling and excavation of rocks in mining and mineral engineering has been conducted by purely mechanical methods. However, the drawbacks of purely mechanical breakage, such as high energy consumption and excessive wear of the tools, severely increase the drilling costs, especially in drilling deep wells in hard formations [1]. These shortcomings and the quest for harnessing deep geothermal energy in cold areas, like Scandinavia, have stimulated an intensive search for non-mechanical drilling and comminution methods. These methods include plasma jet drilling [2], electro-pulse drilling [3-5], microwave induced breakage [6], and thermal shock (flame jet) induced drilling and cracking of rock [7-12].

The thermal shock induced cracking is based on the thermal spallation phenomenon illustrated in Figure 1. Accordingly, when a rock surface is exposed to an intensive heating the resulting thermal gradient (∇T) creates, through local thermal expansion, a compressive stress state (σ), which leads to crack growth in the rock material close to the surface. Spallation, i.e. ejection of rock chips, occurs when the cracks reach the critical length. Rock heterogeneity enhances the spallation or surface damage due mismatching thermal and mechanical properties of rock constituent minerals. Thermal spallation requires about 550-600 °C [1] of

*Author for correspondence (timo.saksala@tuni.fi).
†Present address: Department, Institution, Address, City, Code, Country

temperature to occur in granitic rocks. The laboratory tests of the method have been successful in drilling granite [7-10].

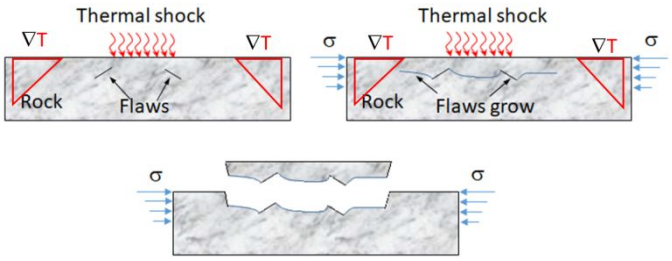

Figure 1. Principle of thermal spallation

However, numerical modelling is needed to further clarify the failure mechanisms and to study the influence of process parameters on the thermal spallation process. Moreover, numerical modelling can help to design and optimize the drill setups and parameters. Previous numerical studies on thermal spallation of rock in particular and thermal jet drilling in general are by Yaseen [10] and Pressacco & Saksala [13] on thermal heating-cooling cycle drilling of rock, by Saksala [14] on thermal spallation of rock, and by Walsh & Lomov [15], and Vogler et al. [16] on thermal spallation. While these studies have their own merits, they are based on the axisymmetric assumption, except the study by Walsh & Lomov [15], which is a 3D study. However, it is a micromechanical study modelling only a small cluster or rock forming grains and concentrating on the failure methods therein. As rock is a heterogeneous material, the axisymmetric assumption is not realistic. Therefore, a genuine 3D study on the full setting of thermal spallation from the application point of view is justified. Moreover, only 3D simulations can provide realistic estimates on the drilling efficiency. It should be mentioned that Mardoukhi et al. [11] presented a 3D numerical study on predicting the heat shock weakening effect on the dynamic tensile strength of granite. However, the thermally induced cracking problem was not properly modelled. Namely. instead of solving the underlying thermo-mechanical problem, the thermally induced damage was assumed in an ad hoc manner.

For these reasons, this paper presents a finite element based numerical study on thermal jet drilling in 3D setting. A numerical solution procedure for the underlying thermo-mechanical problem is developed and validated by the experiments in Mardoukhi et al. [11]. This means that the mechanical dynamic Brazilian disc (BD) test is also simulated for intact and thermally treated rock samples made of Balmoral granite. Then, the method is applied in thermal jet drilling simulation. Finally, the heating-cooling cycle based thermal drilling is simulated.

Theory of the modelling approach

Rock failure model

Rock is modelled as a viscoplastic damaging material, applying a modified version of the model originally presented by Saksala [17]. In this setting, the rock behaviour under loading is isotropic and linear elastic until the elastic limit is reached. Nonlinear softening commences both in compression and tension upon reaching the tensile and compressive uniaxial strengths. The stress states leading to inelastic deformation (strain), are indicated by the usual Drucker-Prager (DR) criterion with the Modified Rankine (MR) criterion as the tensile cut-off by

$$f_{\mathrm{DP}}(\boldsymbol{\sigma},\kappa_{\mathrm{DP}}) = \sqrt{J_2} + \alpha_{\mathrm{DP}} I_1 - k_{\mathrm{DP}} c(\kappa_{\mathrm{DP}}), \quad f_{\mathrm{MR}}(\boldsymbol{\sigma},\kappa_{\mathrm{MR}}) = \sqrt{\Sigma_{i=1}^{3} \langle \sigma_i \rangle^2} - \sigma_{\mathrm{t}}(\kappa_{\mathrm{MR}}) \tag{1}$$

$$c(\kappa_{\mathrm{DP}}) = c_0 + s_{\mathrm{DP}} \kappa_{\mathrm{DP}}, \quad \sigma_{\mathrm{t}}(\kappa_{\mathrm{MR}}) = \sigma_0 + s_{\mathrm{MR}} \kappa_{\mathrm{MR}} \tag{2}$$

where I_1 and J_2 are the first and the second invariants of the stress tensor $\boldsymbol{\sigma}$ and its deviator, respectively, σ_i is the ith principal stress, $\langle\rangle$ are the McAuley brackets, α_{DP} and k_{DP} are the DP parameters, c and σ_{t} are the dynamic cohesion and tensile strength depending on the rates of the internal variables κ_{DP} and κ_{MR}, respectively. The DP parameters are expressed in terms of the friction angle φ: $\alpha_{\mathrm{DP}} = 2\sin\varphi/(3-\sin\varphi)$ and $k_{\mathrm{DP}} = 6\cos\varphi/(3-\sin\varphi)$, enabling to match the uniaxial compressive strength. Moreover, a plastic potential, g_{DP}, of the same form as f_{DP} in (1) but with a dilatation angle $\psi\,(\leq\varphi)$ is also employed to mend the poor prediction of dilatancy of the associated flow rule. Finally, s_{DP} and s_{MR} are the constant viscosity moduli in compression and in tension, respectively.

The damage part of the model is formulated with separate scalar damage variables in compression and tension due to the highly asymmetric behavior of rocks in these stress regions [18]. The damaging is driven by the viscoplastic strain. By this, and the perfect viscoplasticity assumption made above, both the strength and the stiffness degradation both in tension and in compression are governed by the damage part of the model. The damage part of the model is defined by equations

$$\omega_{\mathrm{t}} = A_{\mathrm{t}}\left(1-\exp\left(-\beta_{\mathrm{t}}\varepsilon^{\mathrm{vp}}_{\mathrm{eqvt}}\right)\right),\quad \omega_{\mathrm{c}} = A_{\mathrm{c}}\left(1-\exp\left(-\beta_{\mathrm{c}}\varepsilon^{\mathrm{vp}}_{\mathrm{eqvc}}\right)\right) \tag{3}$$

$$\varepsilon^{\mathrm{vp}}_{\mathrm{eqvt}} = \sqrt{\Sigma_{i=1}^{3}\left\langle\varepsilon_i^{\mathrm{vp}}\right\rangle^2},\quad \varepsilon^{\mathrm{vp}}_{\mathrm{eqvc}} = \sqrt{\frac{2}{3}\boldsymbol{\varepsilon}^{\mathrm{vp}}:\boldsymbol{\varepsilon}^{\mathrm{vp}}},\quad \dot{\boldsymbol{\varepsilon}}_{\mathrm{vp}} = \dot{\lambda}_{\mathrm{DP}}\frac{\partial g_{\mathrm{DP}}}{\partial\boldsymbol{\sigma}} + \dot{\lambda}_{\mathrm{MR}}\frac{\partial f_{\mathrm{MR}}}{\partial\boldsymbol{\sigma}} \tag{4}$$

$$\boldsymbol{\sigma} = (1-\omega_{\mathrm{t}})\boldsymbol{\sigma}_{+} + (1-\omega_{\mathrm{c}})\boldsymbol{\sigma}_{-}\quad(\boldsymbol{\sigma} = \boldsymbol{\sigma}_{+} + \boldsymbol{\sigma}_{-}) \tag{5}$$

$$\boldsymbol{\sigma}_{+} = \max(\boldsymbol{\sigma},0),\quad \boldsymbol{\sigma}_{-} = \min(\boldsymbol{\sigma},0) \tag{6}$$

$$\boldsymbol{\sigma} = \mathbf{E}:\left(\boldsymbol{\varepsilon}_{\mathrm{tot}} - \boldsymbol{\varepsilon}_{\mathrm{vp}} - \boldsymbol{\varepsilon}_{\theta}\right),\quad \boldsymbol{\varepsilon}_{\theta} = \alpha\Delta\theta\mathbf{I} \tag{7}$$

where parameters A_{t} and A_{c} control the maximum values of the damage variables ω_{t} and ω_{c} in tension and in compression, respectively. Parameters β_{t} and β_{c}, controlling the amount of dissipation, are defined so that fixed amount energy, expressed by the mode I and II fracture energies G_{Ic} and G_{IIc}, are dissipated during the softening process irrespective of the element size. Thereby, $\beta_{\mathrm{t}} = \sigma_{\mathrm{t0}}h_{\mathrm{e}}/G_{\mathrm{Ic}}$ and $\beta_{\mathrm{c}} = \sigma_{\mathrm{c0}}h_{\mathrm{e}}/G_{\mathrm{IIc}}$ with h_{e} being a characteristic length of a finite element. The equivalent viscoplastic strain in tension and compression, $\varepsilon^{\mathrm{vp}}_{\mathrm{eqvt}}$, $\varepsilon^{\mathrm{vp}}_{\mathrm{eqvc}}$, respectively, are defined by the rate of viscoplastic strain tensor $\boldsymbol{\varepsilon}_{\mathrm{vp}}$ and its principal values $\varepsilon_i^{\mathrm{vp}}$. The viscoplastic strain tensor is expressed in (4) by the Koiter's bisurface rule for the corner plasticity case, i.e. the case when both yield criteria are violated. Moreover, the nominal-effective stress relationship in (5) is written with the positive-negative parts decomposition. Furthermore, the stress-strain relationship with the elasticity tensor $\mathbf{E}$, is based on the small deformation enabled decomposition of the total strain to elastic, viscoplastic and thermal strain tensors, respectively, as $\boldsymbol{\varepsilon}_{\mathrm{tot}} = \boldsymbol{\varepsilon}_{\mathrm{e}} + \boldsymbol{\varepsilon}_{\mathrm{vp}} + \boldsymbol{\varepsilon}_{\theta}$. In addition, α and $\Delta\theta$ are the thermal expansion coefficient and the temperature change, and $\mathbf{I}$ is the second order identity tensor. The details of the stress integration of the model are dealt with in Saksala [17].

Explicit time stepping scheme for discretized thermo-mechanical problem

This problem of thermal spallation is governed (simultaneously) by the time-dependent heat equation and the equation in motion, which can be written in the finite element discretized form, written at time t as [19]

$$\mathbf{M}_{\mathrm{u}}\ddot{\mathbf{u}}_t + \mathbf{f}_t^{\mathrm{int}} = \mathbf{f}_t^{\mathrm{ext}}\quad\text{with}\quad \mathbf{f}_t^{\mathrm{int}} = \mathbf{A}_{\mathrm{e}=1}^{\mathrm{N_{el}}}\int_{\Omega^{\mathrm{e}}}\mathbf{B}_{\mathrm{u}}^{\mathrm{e},\mathrm{T}}\boldsymbol{\sigma}_t\mathrm{d}\Omega \tag{8}$$

$$\mathbf{M}_{\theta}\dot{\boldsymbol{\theta}}_t + \mathbf{f}_{\theta,t}^{\mathrm{int}} = \mathbf{f}_t^{\Omega} + \mathbf{f}_t^{\Omega}\quad\text{with} \tag{9}$$

$$\mathbf{M}_{\theta} = \mathbf{A}_{e=1}^{N_{el}}\int_{\Omega^e}\rho c\mathbf{N}_{\theta}^{e,T}\mathbf{N}_{\theta}^{e}\Omega^e,\quad \mathbf{f}_{\theta,t}^{\mathrm{int}} = \mathbf{A}_{e=1}^{N_{el}}\int_{\Omega^e}k\mathbf{B}_{\theta}^{e,T}\nabla\boldsymbol{\theta}_t d\Omega^e \tag{10}$$

$$\mathbf{f}_t^{\Omega} = \mathbf{A}_{e=1}^{N_{el}}\int_{\Gamma_q^e}\mathbf{N}_{\theta}^{e}q_n d\Gamma,\quad \mathbf{f}_t^{\Omega} = \mathbf{A}_{e=1}^{N_{el}}\int_{\Omega^e}\mathbf{N}_{\theta}^{e}\mathrm{Q}d\Omega^e \tag{11}$$

where the symbol meanings are as follows: $\mathbf{u}$ is the acceleration vector; $\boldsymbol{\theta}$ temperature vector; $\mathbf{M}$ is the lumped mass matrix; $\mathbf{f}_{\mathrm{ext}}$ is the external force vector, respectively; $\mathbf{f}_{\mathrm{int}}$ is the internal force vector; $\mathbf{C}$ is the capacitance

matrix; $\mathbf{f}_\theta^{\text{int}}$ is the thermal internal force vector; $\mathbf{f}_\theta$ is the external heat loading vector; $\mathbf{f}_Q$ is the mechanical heating term (vector); $\mathbf{A}$ is the standard finite element assembly operator; $\mathbf{B}_e$ is the kinematic matrix (mapping the nodal displacement into element strains); ρ is the density; c is the specific heat capacity; k is the thermal conductivity, θ is the temperature; $\mathbf{N}_\theta$ is the temperature interpolation matrix; k is the conductivity; q_n is the normal component of the heat flux; $\mathbf{B}_\theta$ is the gradient of $\mathbf{N}_\theta$.

The specific heat capacity and conductivity depend on temperature and this dependence is defined later. Moreover, for a damaging material the conductivity depends on the integrity of the material. This dependence is also defined later. In the present problem, heating time is short (< 1 sec) so that the convection at the boundaries of the rock specimen can be ignored as insignificant. Finally, the term Q in (9) represents the mechanical heat production through dissipation and strain rate. This term is insignificant in comparison to the external flux, hence $\mathbf{f}^Q \equiv \mathbf{0}$ from now on.

The thermo-mechanical problem governing the thermal spallation is solved with explicit time marching. The forward Euler method is employed here leading to following equations for the new temperature and mechanical response:

$$\mathbf{M}_\theta \boldsymbol{\theta}_{t+\Delta t} = \mathbf{M}_\theta \boldsymbol{\theta}_t + \Delta t(\mathbf{f}_t^\theta - \mathbf{f}_{\theta,t}^{\text{int}}) \rightarrow \boldsymbol{\theta}_{t+\Delta t} \quad (12)$$

$$\mathbf{M}_u \mathbf{u}_t = \mathbf{f}_t^{\text{ext}} - \mathbf{f}_t^{\text{int}} \rightarrow \mathbf{u}_t \quad (13)$$

$$\mathbf{u}_{t+\Delta t} = \mathbf{u}_t + \Delta t \mathbf{u}_t \quad (14)$$

$$\mathbf{u}_{t+\Delta t} = \mathbf{u}_t + \Delta t \mathbf{u}_{t+\Delta t} \quad (15)$$

The solution procedure starts with solving the temperature by Equation (12). This is followed by an element level loop for solving the new stress, viscoplastic strain, and other internal variables that are used for the assembly of the new internal force vector. Then, the acceleration can be solved with (13) and, finally, the mechanical response is computed further by (14) and (15).

This is an explicit time stepping scheme and thus, unfortunately, only conditionally stable under the Courant stability limit (depending on the smallest element size in the mesh and the wave speed in the media) for explicit time integrators. Moreover, for a given mesh size, the thermal part allows time steps several orders of magnitude larger than the mechanical one. Fortunately, the inertia effects in the problem of thermal jet treatment of rock are so mild that the mechanical part of the problem is particularly amenable to mass scaling.

Numerical examples

Material properties and model parameters

Rock materials are heterogeneous aggregates of different minerals. Moreover, microcracks and imperfect grain boundaries add to the heterogeneity, which is the major factor affecting the rock behaviour under loading. However, in the present finite elements based modelling approach, the rock material is mostly assumed homogeneous. This assumption is justified under dynamic loading conditions since brittle materials behave more deterministically as loading rate increases [20], which means that heterogeneities become less significant. Notwithstanding, heterogeneity expectedly influence the heat shock induced damage processes, which are of modest loading rate. Therefore, the heterogeneity is tested in these simulations by random clusters of finite elements representing different minerals of the rock.

The homogenized material thermal and mechanical properties and the model parameters used in the simulations are given in Table 1. The mechanical properties of the minerals are from Mahabadi [21] while the

thermal properties are from Tufail et al [22] and Heuze [23]. Balmoral granite, considered in the simulations, consists of Quartz (33 %), Potash Feldspar (40 %), Plagioclase Felspar (19), and Biotite and Hornblende (8 %) minerals [11]. However, due to the lack of data on the mechanical and thermal properties for the two types of Feldspars, they are simply lumped together and called Feldspars in Table 1.

Table 1. Material properties and model parameter values

Parameter/mineral	Quartz	Feldspars	Biotite	Homog
E [GPa]	80	60	20	63
σ_{t0} [MPa]	10	8	7	8
σ_{c0} [MPa]	180	180	180	180
ν	0.17	0.29	0.2	0.25
ρ [kg/m^3]	2630	2630	2800	2600
G_{Ic} [J/m^2]	40	40	28	39
G_{IIc} [J/m^2]	2000	2000	1400	1950
φ [°]	50	50	50	50
ψ [°]	5	5	5	5
s_{MR} [MPa·s]	0.25	0.25	0.25	0.25
s_{DP} [MPa·s]	0.3	0.3	0.3	0.3
A_t	0.98	0.98	0.98	0.98
A_c	0.98	0.98	0.98	0.98
α [1/K]	1.60E-5	0.75E-5	1.21E-5	1.067E-5
k [W/mK]	4.94	2.34	3.14	3.26
c [J/kgK]	731	730	770	733.5
f [%]	33	59	8	100

The uniaxial compressive strength of Balmoral granite is 180 MPa. With the friction angle of 50 °, this translates into a cohesion, used in the DP criterion, of $c_0 = (1 - \sin\varphi)/(2\cos\varphi)\sigma_{c0}$ = 32.8 MPa. The viscosity parameter for the pre-peak continuum model, s, is chosen so that the dynamic indirect tensile strength (29±3 MPa) of the Balmoral granite in the experiments reported in [11] can be predicted. The mode II fracture energy values are calculated by multiplying the mode I value with the factor 50. In the present setting, fracture energies represent the energies dissipated during the uniaxial tension and compression softening processes, i.e. the area under the stress-strain curves in these tests – hence the relatively large values of mode II energies.

In the present applications, the temperature rises hundreds of degrees. Therefore, some of the mechanical and thermal properties of rock are assumed temperature dependent. More precisely, Young's modulus, tensile and compressive strengths are assumed to dependent linearly on temperature so that their values at 600 °C are 50 % of the corresponding values at room temperature (20 °C) [22, 23]. Furthermore, thermal conductivity k is also linearly dependent on the temperature so that, at 500 °C, it drops 50 % from the value at room temperature [22, 23]. The specific heat capacity c is assumed constant in this study for computational reasons (there is thus no need to update **C** at every time step) and due to its weaker temperature dependence (it changes only 30 % in this range of temperatures). Mathematically, the temperature dependency of a property x is thus of form $x(\theta) = x(\theta_{\text{ref}}) + K_x^{6u}(\theta - \theta_{\text{ref}})$, where K_x^{6u} is the modulus of temperature dependence and θ_{ref} is reference temperature. The linearity of the temperature dependency of these properties is a decent approximation within this temperature range [10, 19, 22, 23]. However, the temperature dependence of thermal expansion coefficient for granite is not linear [23]. Since it is the key parameter with respect to thermal stresses, its nonlinearity is approximated by a second order polynomial by

$$\alpha(\theta) = a\theta^2 + b\theta + c \quad \text{for } \theta \in [293, 873]\text{K}$$

$$\alpha(\theta) = \alpha_{873} \quad \text{for } \theta > 873 \text{ K} \quad \text{with} \qquad (16)$$
$$a = \frac{\alpha_{873} - \alpha_{293}}{336400}, \quad b = \frac{293(\alpha_{293} - \alpha_{873})}{168200}, \quad c = \frac{250551\alpha_{293} - 85849\alpha_{873}}{336400}$$

where α_{873} and α_{293} are the thermal expansion coefficients at 600 °C and 20 °C for each mineral. The value in Table 1 is taken for α_{293} while $\alpha_{873} = 3.5\alpha_{293}$. This choice approximates well the data collected by Heuze [23] for several granites. It should be noted that beyond 600 °C (i.e. beyond the α-β phase transformation of Quartz) the thermal expansion is assumed constant. This assumption is a compromise between the Quartz behavior, which exhibits a linearly descending trend beyond the α-β phase transformation, and the Feldspar behavior, which increases linearly from the room temperature up to 800 °C [26].

When a material loses its integrity in form of crack opening or void creation, the thermal properties should also change. For simplicity, it is assumed that only the thermal conductivity is affected by mode I damage process. Thereby, the tensile damage variable operates on the conductivity, similarly as on the effective stress, by $k(\theta,\omega_t) = k_\theta(\theta)(1-\omega_t)$, where $k_\theta(\theta)$ is the linear function describing the dependence of bulk conductivity on temperature. At the maximum value of tensile damage, 0.98, the value of k is thus 2 % of its initial value when the temperature is kept constant. Therefore, as the rock material deteriorates, the thermal conductivity value approaches to that of air (~0.025 W/mK). This setting renders the global thermo-mechanical problem coupled, i.e. there is two-way information flow between the mechanical and the thermal parts.

Model validation: plasma jet treatment of granite

The first numerical example presents a validation of the modelling approach against the experiments by Mardoukhi et al. [11]. In the experiments therein, a Brazilian disc sample made of Balmoral granite was one-sidedly treated by a plasma jet (with a nominal power or 50 kW and a jet diameter of 20 mm) moved at constant velocities ranging from 50 mm/s to 100 mm/s and at a distance of 6.5 cm above the rock sample (see Figure 2a). While the temperature of the plasma jet is about 3000 °K at the applied distance from the nozzle [24], there was, unfortunately, no method to measure the surface temperatures of the rock samples during the plasma jet treatment. As the time of exposure is short (< 0.5 s), the surface cools down so fast that measuring the temperature after the exposure is meaningless. For this reason, the results available from these experiments are images under microscope and naked eye, as well as 3D profilometer analyses of the treated surface. Figure 2 show an example of the results for the case with plasma jet treatment velocity of 50 mm/s. Clear spalling damage is attested with the crated depths varying 0.2 to 0.8 mm.

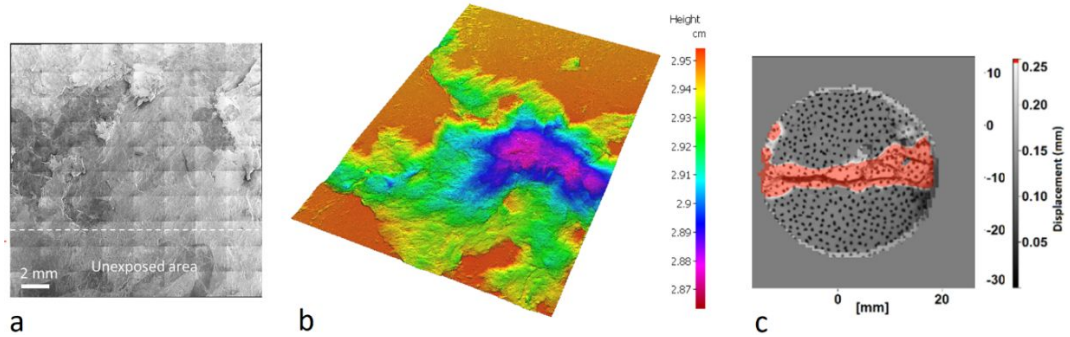

Figure 2. Microscope image on the surface damage on Balmoral granite induced by the plasma jet at 50 mm/s (a), a 3D profilometer analysed surface craters (b), and an example of experimental failure mode of a plasma jet treated BD sample (c) produced with the digital image correlation technique [11].

However, the focus of that study was the weakening effect of thermally induced surface damage on the dynamic tensile strength of granite. Therefore, dynamic Brazilian disc test were carried out on five intact and

five plasma jet treated samples using the Split Hopkinson Pressure Bar device. The indirect dynamic tensile strength for the intact sample was 29±3 MPa at the strain rate of ~12 s^{-1}. Figure 2c shows an example of the failure mode of a plasma jet treated BD sample (50 mm/s) produced with the digital image correlation technique. At the slowest velocity (50 mm/s) of the plasma jet, the dynamic indirect tensile strength was 23±3 MPa (20 % weakening) at the strain rate of ~12 s^{-1}.

An attempt to predict these experiments with the boundary conditions in Figure 2 is presented here. The high velocity flow of air and other particles, being about 100 m/s at the distance applied in the experiments [24], of the jet are ignored in this study. It should however be noted that such velocity facilitates the loose rock material removal from the rock surface.

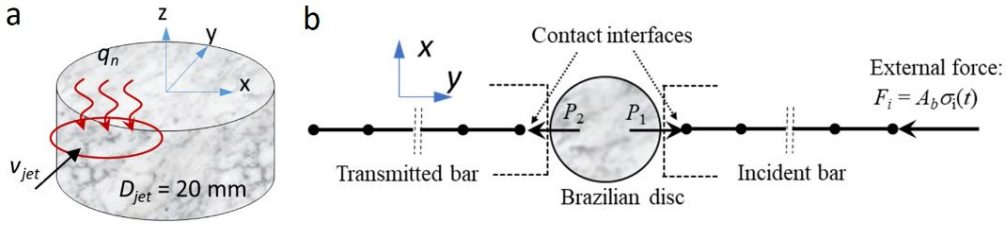

Figure 3. Schematic of the moving plasma jet treatment (a) and dynamic Brazilian disc test (b) simulations.

The principle of the moving thermal flux boundary condition mimicking the plasma jet treatment is shown in Figure 3a. At each time station, the finite element mesh nodes on the top surface of the disc found inside the red circle (the jet) are included in the assembly of the external heat flux vector $\mathbf{f}_\theta$ in Equation (3). The principle of the computational procedure for the numerical Brazilian disc test shown in Figure 3b is as follows. The impact of the striker bar induces a compressive stress wave, which is simulated as an external stress pulse, $\sigma_i(t)$, obtained from the experiments. The incident and transmitted bars are modeled with two-node standard bar elements while the Brazilian disc is discretized with linear tetrahedral elements. Finally, the contacts between the bars and the disc are modeled by imposing kinematic (impenetrability) constraints between the bar end nodes and the disc edge nodes. Mathematically, they are of form $u_{\text{bar}} - u_n = b_n$, where u_{bar} and u_n are the degrees of freedom in axial direction (y-direction in Figure 3) of the bar node and a rock contact node n, respectively, and b_n is the distance between the bar end and rock boundary node. The contact constraints are imposed by using the Lagrange multipliers, corresponding to contact forces P_1 and P_2, which are solved using the forward increment Lagrange multiplier method (see Saksala [17] and Carpenter et al. [25]).

The indirect tensile strength is calculated based on the elasticity solution of the problem of a cylindrical disc under diametrical compression:

$$\sigma_T = \frac{2F}{\pi LD}, \quad F = \frac{1}{2}(P_1 + P_2), \quad P_1 = A_b E_b(\varepsilon_i + \varepsilon_r), \quad P_2 = A_b E_b \varepsilon_t \tag{16}$$

where F is the force acting on the sample with length (thickness) L and diameter D being L = 20 mm and D = 40 mm in the present case. Force F can be calculated from strains measured by strain gages from either of the bars or taken, as in (16), as an average of the forces P_1 and P_2 which are calculated, respectively, by the sum of the incident and reflected strain signals ($\varepsilon_i + \varepsilon_r$) and by the transferred strain signal (ε_t), using the bas cross section (A_b) and the Young's modulus (E_b) of bar material.

There was no method available to the authors to determine the actual thermal flux (power) in the experiments. Therefore, a resort to the trial and error method testing different values of flux intensity producing the desired result was necessary. The plasma jet movement velocity is set to 50 mm/s. Figure 4 shows the results of the

plasma jet simulations for flux intensities q_n = 1 MW/m^2 and q_n = 1.25 MW/m^2 with a uniform mesh consisting of 206739 linear tetrahedral elements.

With the lower flux intensity, temperature rise at the flux nodes (i.e. the nodes were the moving flux was directly applied) reaches about 350 °C followed by rapid (natural) cooling (Figure 4c). Temperature rises only in a very narrow layer adjacent to the disc surface due to the movement of the jet, as attested in Figure 4b showing the temperature field at t = 0.75 s. Due to this very steep and local temperature gradient, significant tensile damage, reaching 0.8 at many elements, is induced (see Figure 4a). With the higher flux intensity, resulting in maximum temperatures of ~500 °C at the flux nodes (Figure 4f), tensile damage values reach the maximum (0.98), and even some localisation patterns can be observed in Figure 4d. Figure 4e, where the elements at which tensile damage exceeds 0.9 are plotted, show the extension of damage in this case. The temperature profile in Figure 4f show some anomalies, deviating from the general trend, at the exit edge of the disc surface. This overshooting, with temperature reaching even 1000 °C, is due the temperature and damage dependence of the thermal properties. Compressive damage was insignificant in this type of loading.

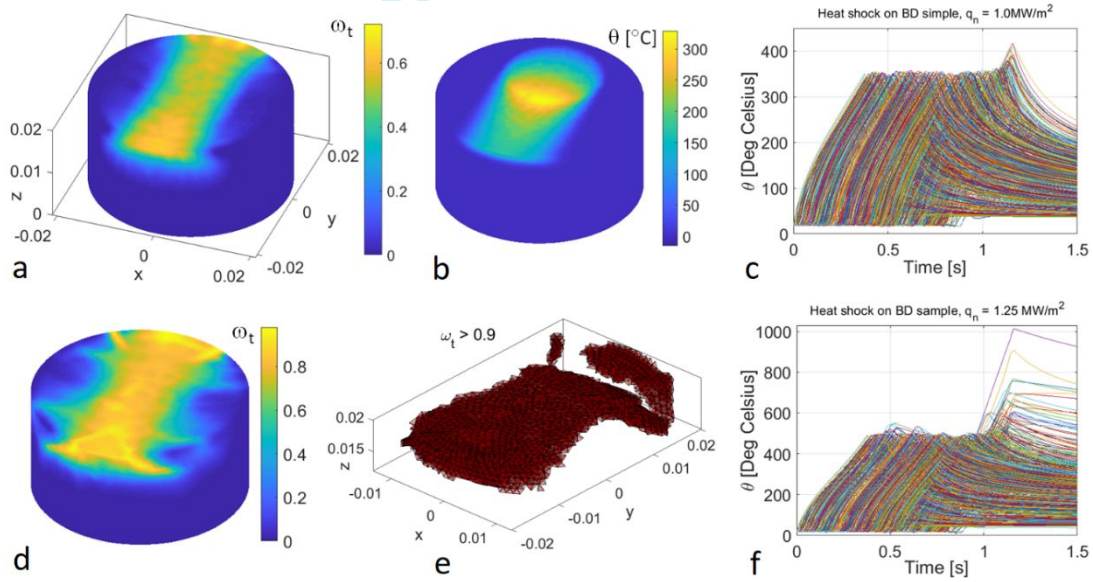

Figure 4. Simulation results for plasma jet treatment: Tensile damage distribution at t = 1.5 s (a), temperature distribution at t = 0.75 s (b), and temperature evolution at the flux nodes (c) with q_n = 1 MW/m^2; tensile damage distribution at t = 1.5 s (d), elements with ω_t > 0.9 (e), and temperature evolution at the flux nodes (f) with q_n = 1.25 MW/m^2.

It should be noted that mass scaling of 10000-fold material density for the mechanical part of the problem was applied here. This allowed for a time step 100-fold larger (~10^{-6} s) than with the original density (~10^{-8} s) for the mesh with 1 mm of average element size. The same problem was simulated with a heating time 10 shorter, i.e. 0.01 s, and with a flux of 12 MW/m^2 using 1000000-fold density. The results (the presentation is omitted for the sake of brevity) for damage and displacement fields were still identical upon eye inspection. The norm of the tensile damage vector (with a maximum value of 0.814), having the final values of damage for each element, was 38.1477, while with the 10000-fold and 1000000-fold mass scaling the norm were 38.1636 (-0.04 % error) and 37.7025 (1.2 % error), respectively. Therefore, it can be concluded that all the simulations with the 10000-fold scaling are reliable. Figure 5 shows the simulation results of the dynamic Brazilian disc tests on the intact and plasma treated rock.

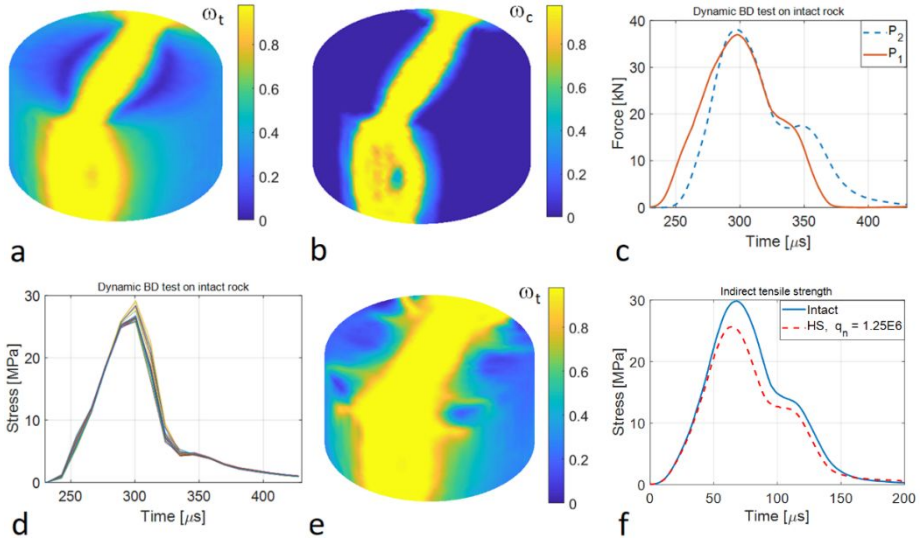

Figure 5. Simulation results for dynamic BD test: Tensile (a) and compressive (b) damage distribution at t = 1.5 s, contact forces (c) and true tensile stresses (in a patch of elements at the centre of the disc) (d) as a function of time for intact rock; tensile damage distribution (e) for plasma jet treated disc with q_n = 1.25 MW/m² (e), and the indirect tensile stresses as a function of time (f) for both cases.

The damage fields in Figure 5a and b display the experimental axial splitting mode, albeit with a very wide localization band (the damaged zone). This wide localization zone is typical for viscoplasticity models resulting from using relatively large values of viscosity moduli required to capture the strain rate hardening effect. Moreover, the contact forces in Figure 5c are in reasonable balance fulfilling the requirement of "dynamic equilibrium" of the dynamic BD test [18]. Therefore, the indirect dynamic tensile stress can be calculated by Equation (5), being shown in Figure 5f. For the intact rock, the indirect tensile strength is 30 MPa which is clearly within the experimental bounds 29±3 MPa for this case [11]. The "true" tensile stresses recorded in a patch of elements at the disc top surface centre attest values, shown in Figure 5d, reasonably close to that calculated by Equation (5). Figure 5e shows the final tensile damage distribution for the plasma jet treated (case q_n = 1.25 MW/m²) numerical rock, which still exhibits the axial splitting mode, as does the experiment [11], albeit with a much wider damaged zone than the experimental one in Figure 2c. The corresponding indirect tensile strength is 25.6 MPa (see Figure 5f). This is value is just below the experimental upper limit (26 MPa) mentioned above. With the lower flux intensity (1 MW/m²), the indirect tensile strength was 27.8 MPa. Keeping in mind the inherent weakness of the continuum approach to capture fracture processes involving discontinuities (cracks), it can however be concluded that the present model can capture the main features of the present problem under both mechanical and thermal loading. Moreover, the simulations suggest that the mere surface damage visible in Figure 2 is not enough to explain the weakening effect on the dynamic indirect tensile strength but there should be internal damage in form of microcracks in the plasma treated samples. However, the resolution of the 3D X-ray tomography device available to the authors was not high enough to detect these cracks. In any case, this correct prediction of the thermal jet weakening effect on the dynamic tensile strength constitutes an indirect validation of the present method, in addition to the direct validation in the form of induced surface damage in Figure 4d and e. Finally, it should be admitted that the present model is better suited to describe the damage due to the thermal loading (Figure 4) than the macrocracks due to high rate mechanical loading (Figure 5).

Thermal drilling

Selected representative simulations of the external heat flux induced thermal drilling of rock with a more realistic setting (a stable thermal jet) are presented here. The basic problem to be numerically studied is the single thermal pulse induced damage on the rock surface. For this method to be competitive, in terms of the rate of penetration, with the mechanical drilling techniques, the heating time must be short and thus the flux intensity extremely high to cause significant damage. Therefore, the heating time is set to 0.1 s followed by a natural cooling of 0.1 s (convection coefficient h_{air} = 10 W/m^{2}K).

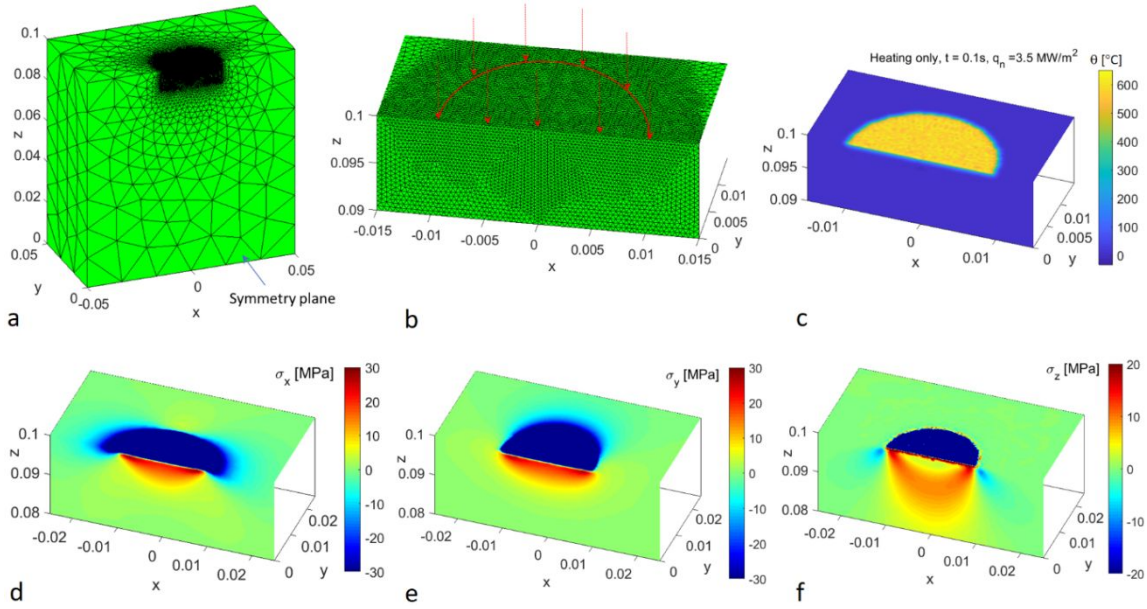

Figure 6. Finite element mesh (exploiting symmetry, unit of axis dimensions [m]) with 210709 tetrahedrons (a) with a detail (b), and simulation results for heating homogeneous linear elastic rock (q_n = 3.5 MW/m^2): temperature field (c) and stress components σ_x (d), σ_y (e), σ_z (f) at the end of the heating stage (t = 0.1 s).

Figure 6a and b shows the finite element mesh (exploiting half-symmetry) and the area where the heat flux is applied. The external thermal jet boundary condition is applied in an area with a radius of 10 mm. Due to the short heating time restricting the temperature rise to the immediate vicinity of the flux the rest of the rock boundaries are assumed perfectly insulated. A flux intensity of 3.5 MW/m^2 is applied in the first simulation instantaneously and then set off at 0.1 s (followed by natural cooling). However, it is first instructive to see the thermal stress components induced by the heating stage only with a linear elastic material. These are shown, along with the temperature field, in Figure 6c-f.

According to the predicted temperature field at the end of heating (Figure 6c), temperature rise is restricted into a very narrow zone just beneath the heated surface. However, the temperatures reach 600 °C at some nodes. Consequently, the ensuing thermal stress components in Figure 6d-f display triaxial (but not hydrostatic) compression state in the heated zone. Magnitude of in-plane (x and y) stresses therein reach -400 MPa while the out-of-plane component reaches -100 MPa. Below the compressed zone, the stress components are in tension reaching 30 MPa. This justifies the choice of the MR criterion for modelling this problem. This 3D stress state also justifies the rationale behind the schematic presentations of thermal spalling phenomenon, such as that in Figure 1. More precisely, the disc or circular plate shaped piece of rock under triaxial compression buckles or ejects out of the rock surface as the material just below fails in mode I due to the tensile stress state therein.

Next, the same simulation is carried out with the cooling phase for the homogeneous material properties including the viscoplastic and damage effects. The results are shown in Figure 7. The temperature evolution at

the flux nodes in Figure 7d show that after reaching the maximum values varying 180 to 650 °C, the temperatures decrease rapidly via natural cooling. The cooling also induces considerable amount of damage in the elements connected to the heated surface, as can be observed by comparing the tensile damage plots at the end of heating in Figure 7a and at the end of cooling in Figure 7c. This is due to a reversal of the of the stress state during cooling [10, 13]. Figure 7b shows the elements where tensile damage exceeds 0.5 at the end of heating. This is the subsurface layer of rock undergoing tensile failures due to tensile stresses therein (see Figure 6d-f).

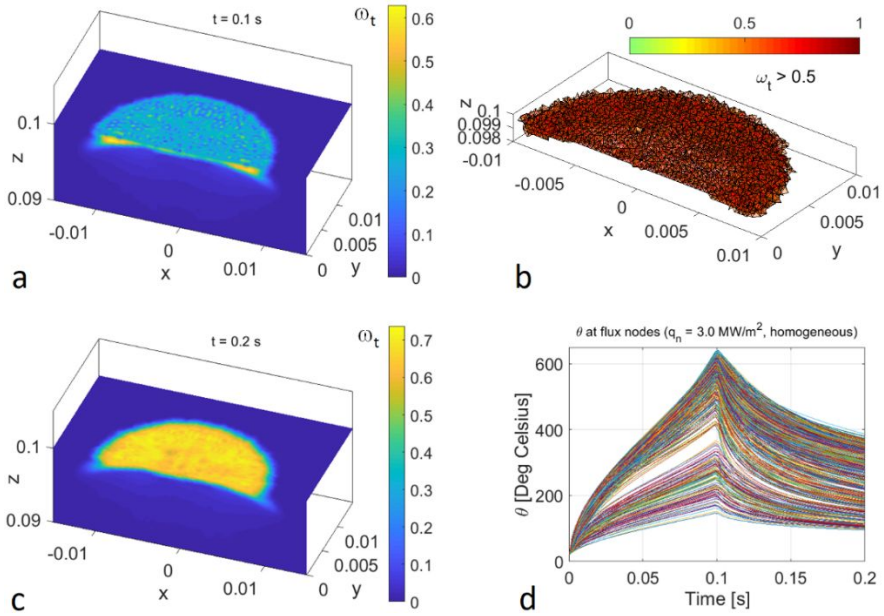

Figure 7. Simulation results for thermal drilling (q_n = 3.0 MW/m², homogeneous rock, axis dimensions in [m]): Tensile damage distribution (a) and the elements with tensile damage > 0.5 (b) at the end of heating, tensile damage at the end of cooling (c) and the temperature evolution at the flux nodes (d).

The compressive damage due to heating was negligible (< 0.1) despite the high compressive stresses. The reason for this is the relatively high friction angle (50°) of the present rock. When the friction angle is lower, say 30°, the rock surface failed in compression as well. Next, the same simulation is carried out with the heterogeneous material properties. The results are shown in Figure 7.

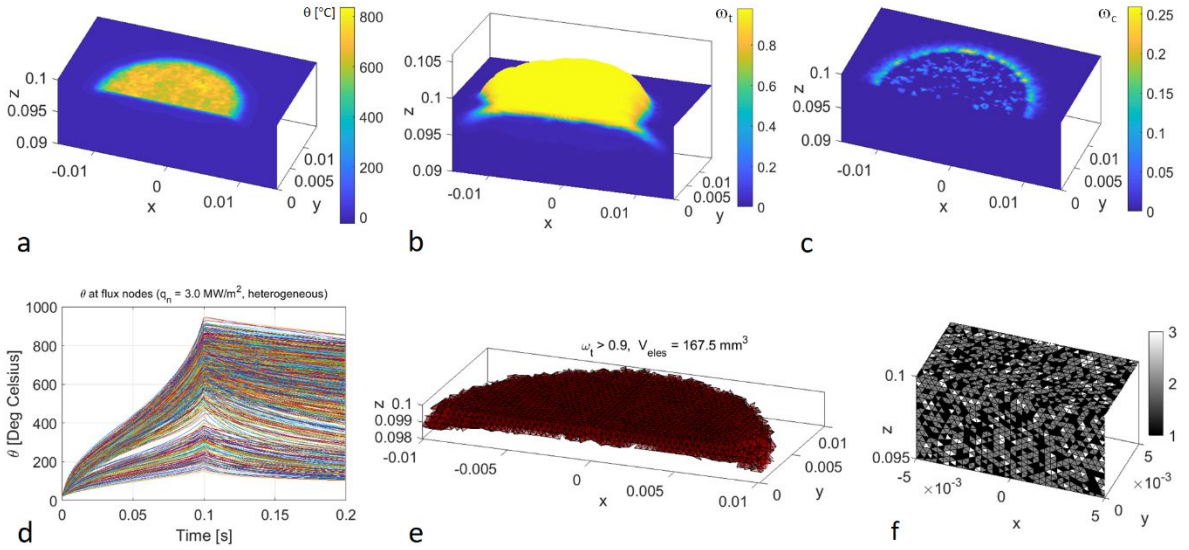

Figure 8. Simulation results for thermal drilling (q_n = 3.0 MW/m², heterogeneous rock, axis dimensions in [m]): Temperature (a), tensile damage (deformed mesh with magnification factor of 20) (b) and compressive damage (c) distribution at the end of cooling, temperature evolution at the flux nodes (d), the elements with tensile damage > 0.9 (e), and the mineral distribution (1 = Quartz, 2 = Felspar, 3 = Biotite) (f).

Heterogeneity, described here as random clusters of finite elements representing different minerals (see Figure 8f), has a substantial effect on the solution features in this problem. First, the temperatures exhibit wider deviation at the flux nodes, as observed in Figure 8a and d. Second, the heterogeneity has increased significantly both the tensile and compressive damage, as attested in Figure 8b and c. Figure 8b shows the tensile damage in the deformed mesh (magnification factor 20), which clearly shows the 3D shape of outward ejection or spallation failure mode. It should, however, be admitted that this predicted excessive localized deformation does not exactly represent experimental spallation (as it manifests in reality) but its standard finite element replication. The volume of elements where the tensile damage variable exceeds 0.9 is 167.5 mm^3 (Figure 8e), which can be interpreted as the volume of removed rock material. This translates, when taking the symmetry into account, assuming 5 heating pulses per second, and assuming the removed rock to have a shape of a penny (quite true based on Figure 8e), into the rate of penetration of $2 \cdot 5 \cdot 60\text{s}/\pi R^2 = 320$ mm/min. It should be noted that this threshold value of 0.9 is chosen only for demonstrative purposes. However, it is somewhat conservative, i.e. smaller values would give more optimistic ROP predictions.

In passing it is also noted that no element deletion was applied here for the convenience sake. This is justified by the applied explicit global solution process and the damage modelling approach, which means that the effect of elements with damage values close to 1 on the solution of the mechanical part is negligible since the nominal stress, which goes to the internal force calculation, for the highly damaged elements is almost zero. Moreover, element deletion would lead to disappearance of mass and hence the violation of the conservation of mass principle

Next, another cycle of heating and natural cooling (pulse2) is simulated setting the final state from the previous simulation (Figure 8) as an initial state for the second cycle simulation. The element faces upon which the heat flux is acting is determined by searching the common facets of the elements with tensile damage exceeding 0.9 (Figure 8e), i.e. the elements considered as removed while not actually deleted, and the rest of the elements. As noted earlier, the elements above this new to-be-heated surface do not affect much the mechanical part of the modelling, as their damage variable values are close to 1 (0.98). The model and material parameters as well as simulation parameters are the same in the first cycle simulation. The results for the temperature evolution at the fluxnodes and the elements with $\omega_t > 0.9$ are shown in Figure 9.

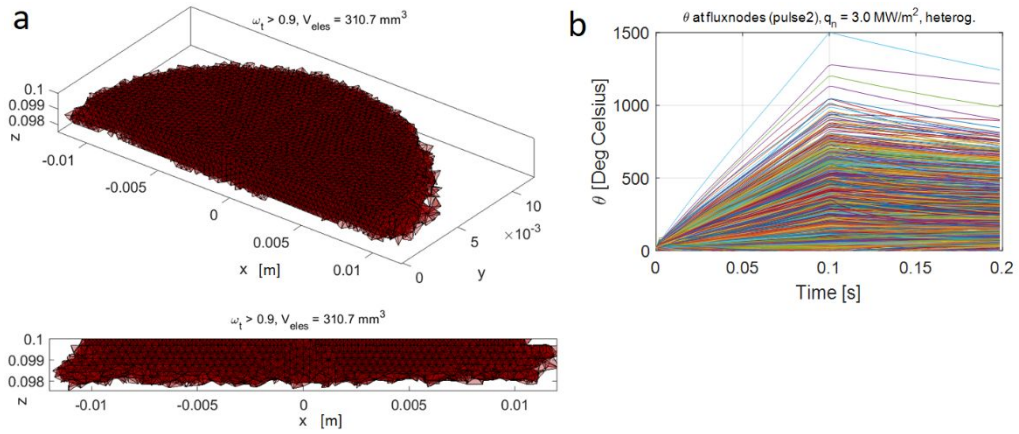

Figure 9. Simulation results for thermal drilling with pulse2 (q_n = 3.0 MW/m^2, heterogeneous rock): The elements with tensile damage > 0.9 (a) and temperature evolution at the flux nodes at the end of cooling (b).

Due to the non-smooth heated surface and the initial damaged state of the material (the elements adjacent and below the ones with $\omega_t > 0.9$ are also damaged), the evolution of temperatures at the fluxnodes (see Figure 9b) are even more non-uniform than during the first heating-cooling cycle simulation in Figure 9. It should be noted that the initial temperatures at the fluxnodes are practically the same as the initial temperature for the first cycle, i.e. 293 K. This is due to the slow nature of temperature conduction in the rock material. As to the volume of damaged elements, 310.7 mm^3, it increases 85 % from that of the first cycle. The borehole then, with a depth of 2 mm, is the complement of the damaged elements in Figure 9.

The final simulation concerns the case where the rock mass is hot, which is the case in drilling deep wells or drilling close to a hot spot in areas with shallow geothermal activity (e.g. Iceland). In such a case, it seems efficient and economical to use combined heating-cooling cycles [10, 13]. There is thus no need to heat the rock as much as when drilling a "cold" rock since the rapid cooling, say by water, can be used to reverse the stress state. A simulation applying first a heating phase of 0.1 s (with q_n = 2.0 MW/m^2) followed by forced cooling by water of 0.1 s duration. The rock bulk temperature is 200 °C, and the cooling is modelled as a convection boundary condition with the heat transfer coefficient h_{water} = 14000 W/m^{2}K [10]. The results are shown in Figure 10.

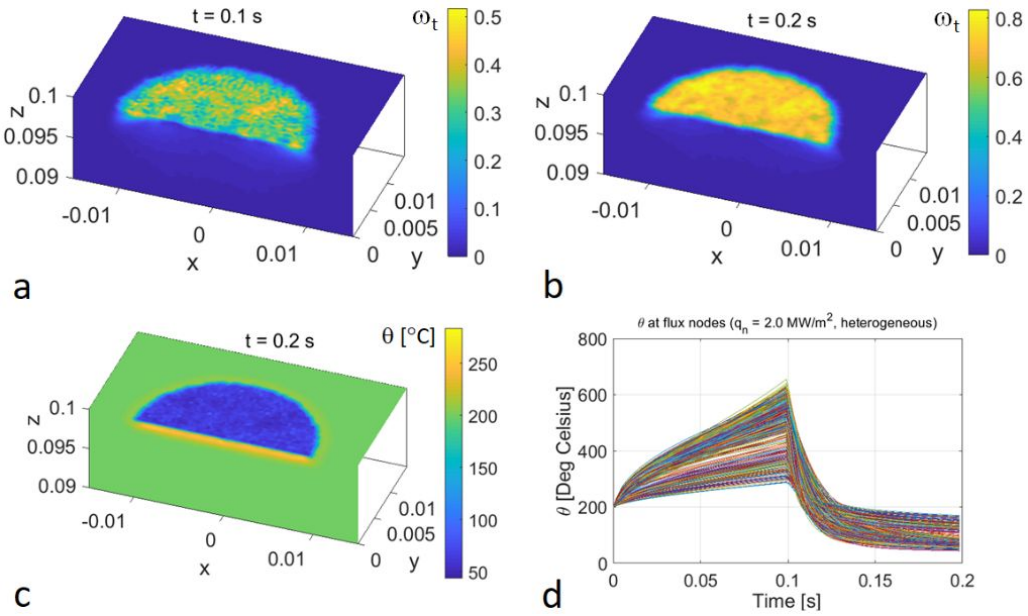

Figure 10. Simulation results for heating-cooling drilling (q_n = 2.0 MW/m², heterogeneous rock, θ_0 = 200 °C, axis dimensions in [m]): Temperature (a), tensile damage (deformed mesh with magnification factor of 20) (b) and compressive damage (c) distribution at the end of cooling, temperature evolution at the flux nodes (d).

With the lower thermal flux intensity, starting from 200 °C initial temperature of the rock mass, the final temperatures at the flux range from 300 °C to 650 °C at the end of heating. The resulting tensile damage at the end of heating reaches 0.5 at many spots (Figure 10a). After the rapid forced cooling, the temperatures at the surface drop down well below the bulk temperature. This temperature drop reverses the stress state from compression to tension, as the results of thermal contraction of the cooled zone. Consequently, more tensile damage is induced, and the resulting condition of rock is quite like that when heating with the higher flux intensity from the room temperature (Figure 7c). Therefore, the heating-cooling drilling is a viable method when the rock mass is hot.

Conclusions

A numerical study on thermal jet drilling exploiting the thermal spallation phenomenon exhibited by granite was carried out. The governing discretised system of equations was solved with explicit time stepping. While this substantially facilitated the solution of the problem with temperature dependent material properties and damage, and ultimately displacement, dependent thermal conductivity, it also imposed a severe restriction on the critical time step of the mechanical part of the system of equations. Fortunately, the mechanical part of the problem admitted extreme mass scaling of using 10000-fold density (even 100000-fold with a minor error), which increased the critical time step to 100-fold allowing practically convenient solution times. It is the relatively low loading rate nature of the thermal loading that renders the mechanical part amenable to mass scaling.

The 3D simulations of the thermal jet drilling corroborated the already experimentally established fact that this method is a viable one with granite rock. Rock heterogeneity has a significant effect facilitating the underlying thermal spallation phenomenon. More precisely, a test simulation using a heat flux, modelling a thermal jet with 10 mm of radius, with an intensity of 3 MW/m² and a duration of 0.1 s, followed by 0.1 s natural cooling phase, showed that significant rate of penetration, ~300 mm/min, can be theoretically achieved. This is a novel result possible to be achieved only through genuine 3D simulations. Finally, a test

simulation exploiting heating-forced cooling cycle demonstrated that this method is more economical in heated rock mass since sufficient damage levels can be achieved when the heated zone is rapidly cooled down to a temperature lower than that of the surrounding rock mass. It can be concluded that the present model can serve as valuable numerical tool for the research and development of thermal jet drilling.

Data accessibility
This article has no additional data.

Author's contributions
TS conceived the idea of this work and performed the numerical analyses. TS also wrote the first draft of the paper. AM and MH performed the experimental work. RK contributed to the thermo-mechanical modelling issues. All authors contributed to the analysis of the results and the final form of the paper.

Competing interests
We declare we have no competing interests.

Funding
This research was funded by Academy of Finland under grant number 298345.

References

1. Chapter 6 Drilling Technology and Costs [Internet]. egs_chapter_6.pdf document available from [cited 20th March 2020] https://www1.eere.energy.gov/geothermal/pdfs/egs_chapter_6.pdf
2. Kocis I, Kristofic T, Gebura, Horvath G, Gajdos M, and Stofanik V. 2017. Novel deep drilling technology based on electric plasma developed in Slovakia *2017 XXXIInd General Assembly and Scientific Symposium of the International Union of Radio Science (URSI GASS)*, Montreal, QC, 2017, pp. 1-4.
3. Andres U. 1995. Electrical disintegration of rock. *Min Proc Ext Met Rev*. **14**, 87-110. (doi.org/10.1080/08827509508914118)
4. Schiegg HO, Rødland A, Zhu G, Yuen DA. 2015. Electro-Pulse-Boring (EPB): Novel Super-Deep Drilling Technology for Low Cost Electricity *J. Earth Sci.* **26**, 37–46. (doi.org/10.1007/s12583-015-0519-x)
5. Yudin AS, Zhurkov My, Martemyanov SM, Datskevich SYu, Vazhov VF. 2017. Electrical discharge drilling of granite with positive and negative polarity of voltage pulses *Int J Rock Mech Min Sci* **123**, 104058. (doi.org/10.1016/j.ijrmms.2019.104058)
6. Hassani F, Nekoovaght PM, Gharib N. 2016. The influence of microwave irradiation on rocks for microwave-assisted underground excavation *J Rock Mech Geotech Eng* **8**, 1-15. (doi.org/10.1016/j.jrmge.2015.10.004)
7. Kant MA and von Rohr PR. 2016. Minimal Required Boundary Conditions for the Thermal Spallation Process *Int J Rock Mech Min Sci* **84**, 177-186. (doi.org/10.1016/j.ijrmms.2015.12.009)
8. Rossi E, Kant MA, Madonna C, Saar MO, von Rohr PR. 2018. The Effects of High Heating Rate and High Temperature on the Rock Strength: Feasibility Study of a Thermally Assisted Drilling Method *Rock Mech Rock Eng* **51**, 2957-2964. (doi.org/10.1007/s00603-018-1507-0)
9. Kant MA, Rossi E, Madonna C, Höser D, von Rohr PR. 2017. A theory on thermal spalling of rocks with a focus on thermal spallation drilling *J. Geophys. Res. Solid Earth*. **122**, 1805-1815. (doi:10.1002/2016JB013800)
10. Yaseen M. 2014. Use of thermal heating/cooling process for rock fracturing: numerical and experimental Analysis, Dissertation, University of Lille.
11. Mardoukhi A, Saksala T, Hokka M, Kuokkala V-T. 2017. A numerical and experimental study on the tensile behavior of plasma shocked granite under dynamic loading *Rakenteiden Mekaniikka (Journal of Structural Mechanics)* **50**, 41-62. (doi.org/10.23998/rm.65301)

12. Mardoukhi A, Mardoukhi Y, Hokka M, Kuokkala V-T. 2017. Effects of strain rate and surface cracks on the mechanical behaviour of Balmoral Red granite *Phil Trans R Soc A* 37520160179. (http://doi.org/10.1098/rsta.2016)
13. Pressacco M, Saksala T. 2019. Numerical modelling of rock drilling by rapid thermal heating-cooling process. In: Fontoura SD, Rocca RJ, Mendoza JP (Eds.). Rock Mechanics for Natural Resources and Infrastructure Development - Full Papers. *Proceedings of the 14th International Congress on Rock Mechanics and Rock Engineering (ISRM 2019)*, September 13-18, 2019, Foz do Iguassu, Brazil: CRC Press, London.
14. Saksala T. 2018. Numerical modelling of thermal spallation of rock. Mecánica Computacional Vol XXXVI, págs. 1567-1574 (artículo completo) José G. Etse, Bibiana M. Luccioni, Martín A. Pucheta, Mario A. Storti (Eds.) San Miguel de Tucumán, 6-9 Noviembre 2018. Proceedings of XII Argentine Congress on Computational Mechanics (MECOM2018), 6-9 November 2018, Tucuman, Argentina.
15. Walsh SDC, Lomov IN. 2013. Micromechanical modeling of thermal spallation in granitic rock. *Int J Heat Mass Transfer* **65**, 366–373. (doi.org/10.1016/j.ijheatmasstransfer.2013.05.043)
16. Vogler D, Walsh SDC, von Rohr PR, Saar M. 2020. Simulation of rock failure modes in thermal spallation drilling *Acta Geotech.* (Published online) (doi.org/10.1007/s11440-020-00927-7)
17. Saksala T. 2010. Damage–viscoplastic consistency model with a parabolic cap for rocks with brittle and ductile behavior under low-velocity impact loading *Int J Numer Anal Meth Geomech* **34**, 1362-1386. (doi: 10.1002/nag.868)
18. Zhang QB, Zhao J. 2014. A review of dynamic experimental techniques and mechanical behaviour of rock materials *Rock Mech Rock Eng* **47**, 1411–1478. (doi.org/10.1007/s00603-013-0463-y)
19. Ottosen NS, Ristinmaa M. 2005. The Mechanics of Constitutive Modeling. Elsevier: Amsterdam.
20. Denoual D, Hild F. 2000. A damage model for the dynamic fragmentation of brittle solids. *Comput Method Appl M* **183**, 247–258. (http://dx.doi.org/10.1016/S0045-7825(99)00221-2)
21. Mahabadi OK. 2012. Investigating the influence of micro-scale heterogeneity and microstructure on the failure and mechanical behaviour of geomaterials. Dissertation, University of Toronto.
22. Tufail M, Shahzada K, Gencturk B, Wei J. 2017. Effect of Elevated Temperature on Mechanical Properties of Limestone, Quartzite and Granite Concrete *Int J Concr Struct M* **11**, 17-28. (doi.org/10.1007/s40069-016-0175-2)
23. Heuze F 1983 High Temperature Mechanical, Physical and Thermal Properties of Granitic Rocks – A Review. *Int J Rock Mech Min Sci & Geomech Abstr* **20**, 3-10. (doi.org/10.1016/0148-9062(83)91609-1)
24. Pawlowski L. 2008. The Science and Engineering of Thermal Spray Coatings, 2nd Edition, John Wiley & Sons Ltd, Chichester.
25. Carpenter NJ, Taylor RL, Katona MG. 1991. Lagrange Constraints for Transient Finite Element Surface Contact. *Int J Numer Meth Eng*. **32**, 103-128. (doi.org/10.1002/nme.1620320107)
26. Shang X, Zhang Z, Xu X, Liu T, Xing Y. 2019. Mineral Composition, Pore Structure, and Mechanical Characteristics of Pyroxene Granite Exposed to Heat Treatments. *Minerals* **9**, 553. (doi.org/10.3390/min9090553)

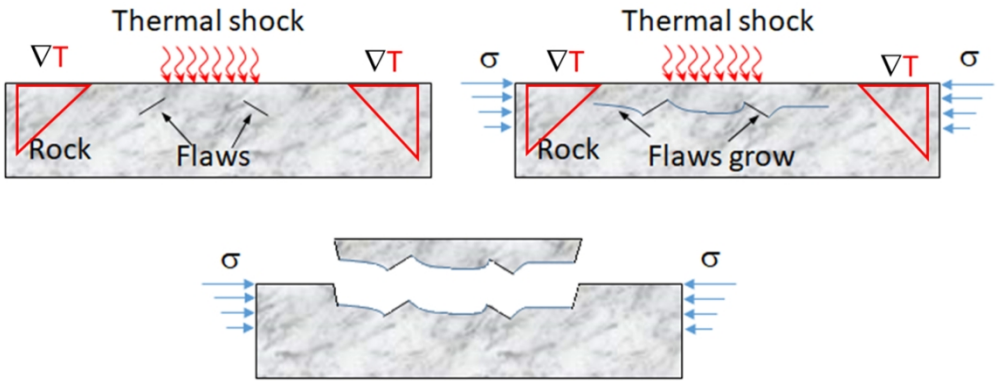

272x104mm (120 x 120 DPI)

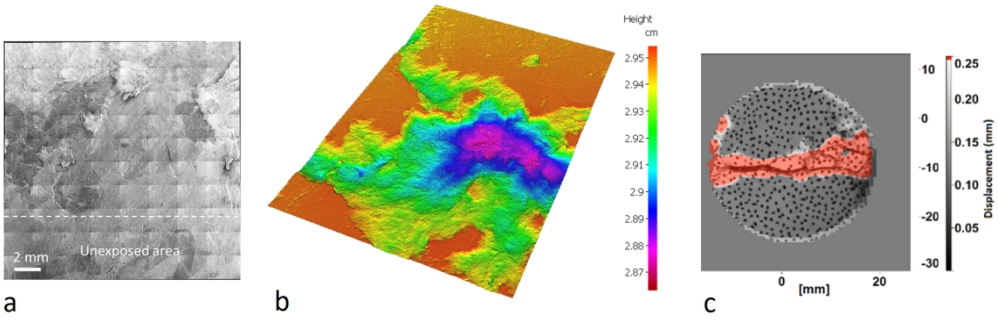

421x133mm (120 x 120 DPI)

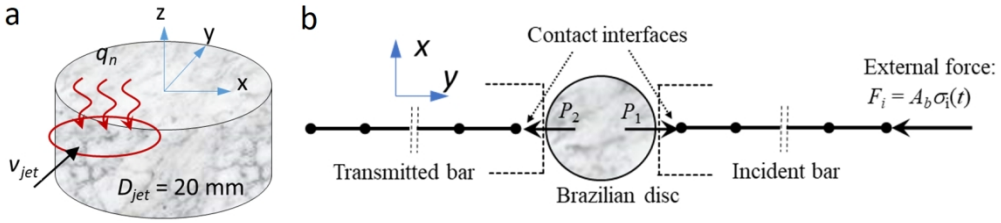

367x81mm (120 x 120 DPI)

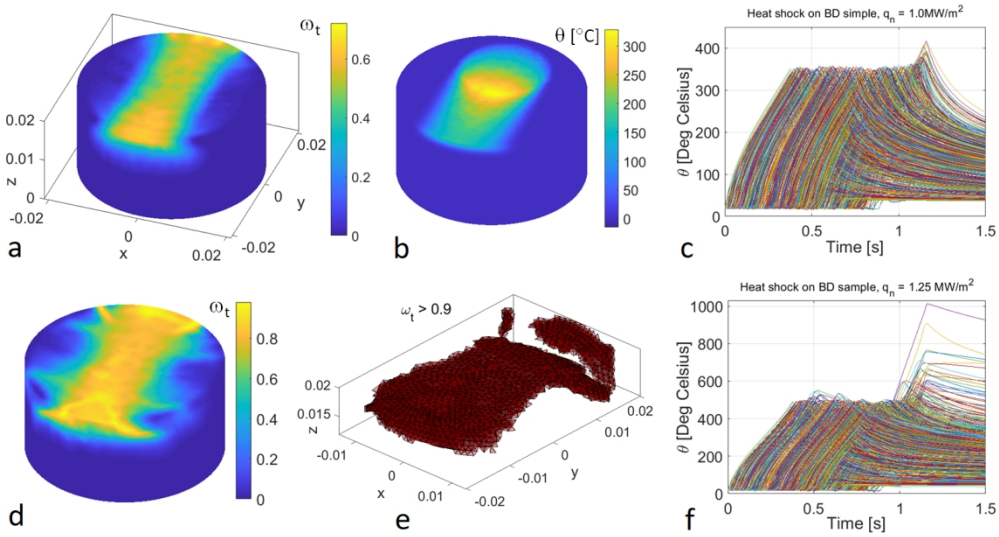

345x183mm (120 x 120 DPI)

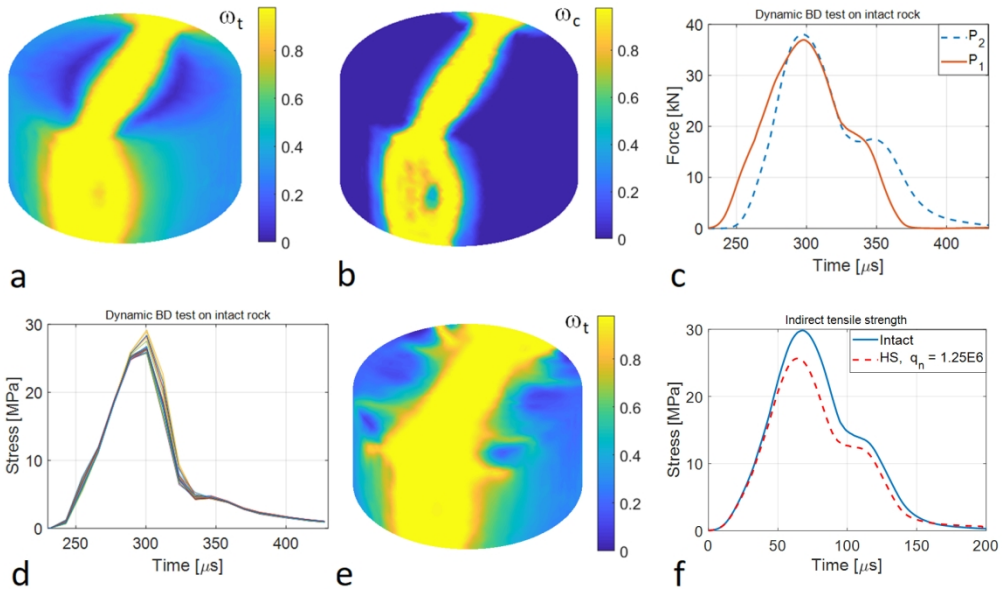

389x228mm (120 x 120 DPI)

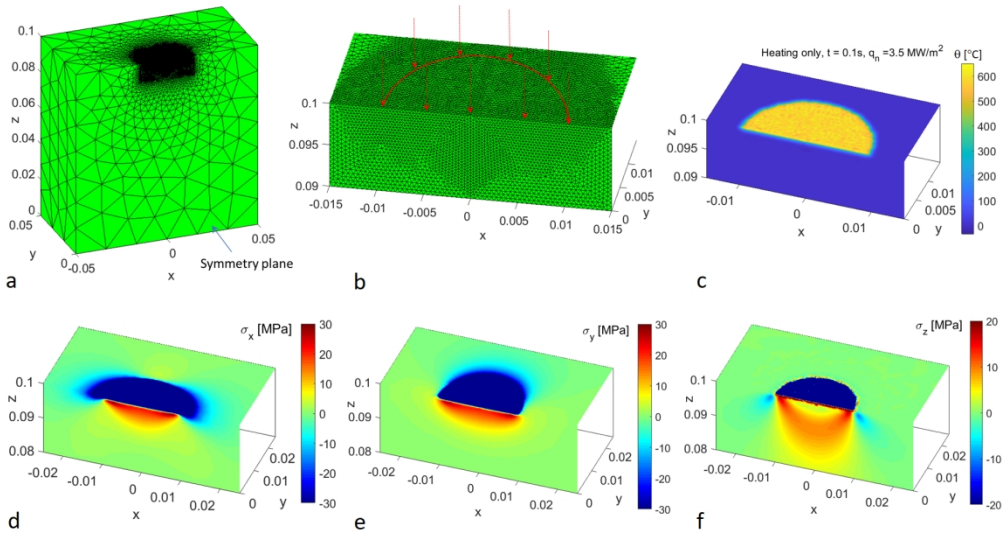

406x215mm (120 x 120 DPI)

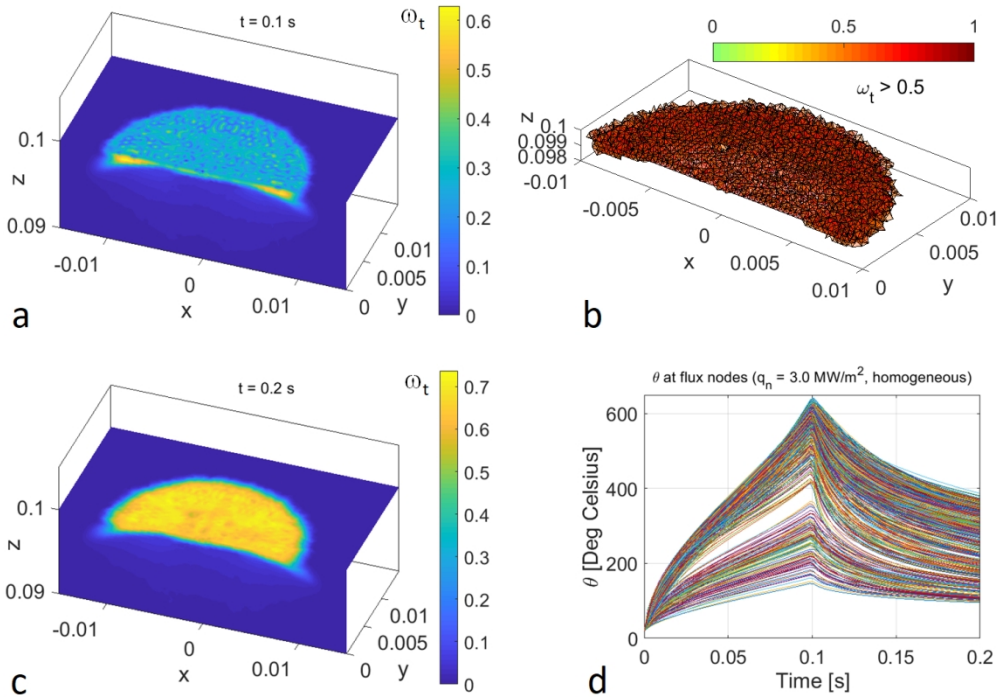

318x221mm (120 x 120 DPI)

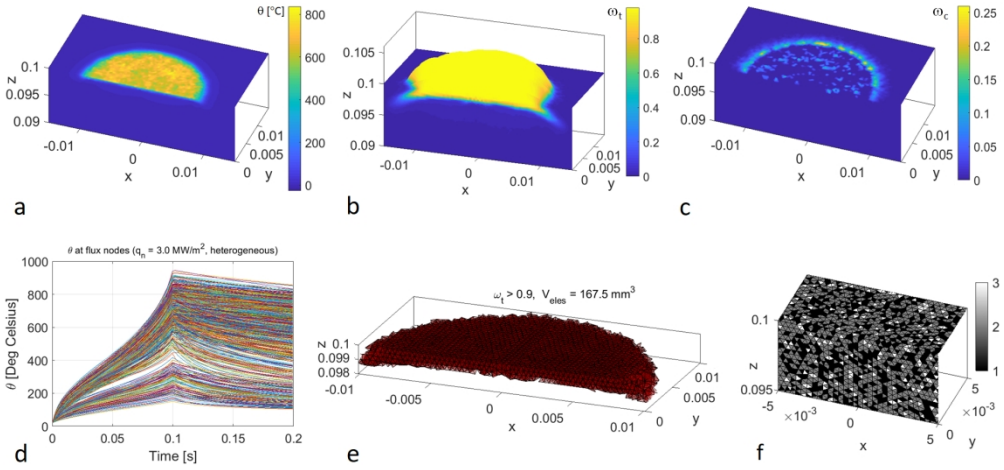

417x193mm (120 x 120 DPI)

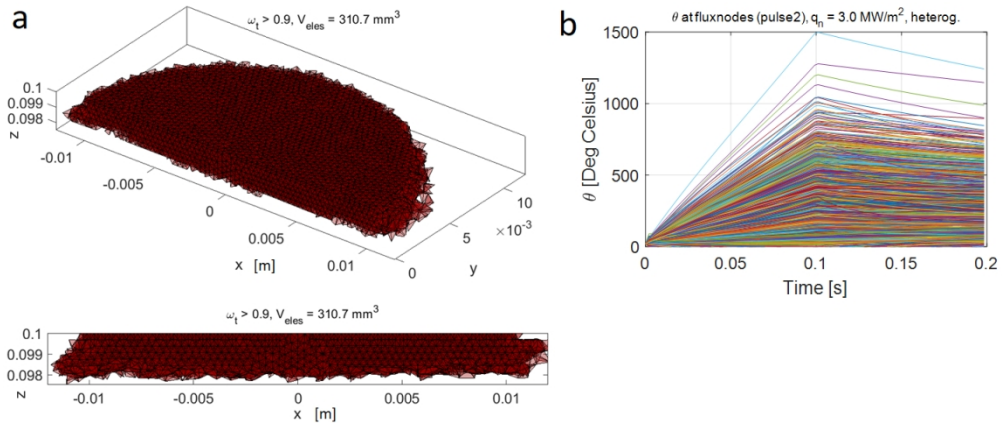

302x127mm (120 x 120 DPI)

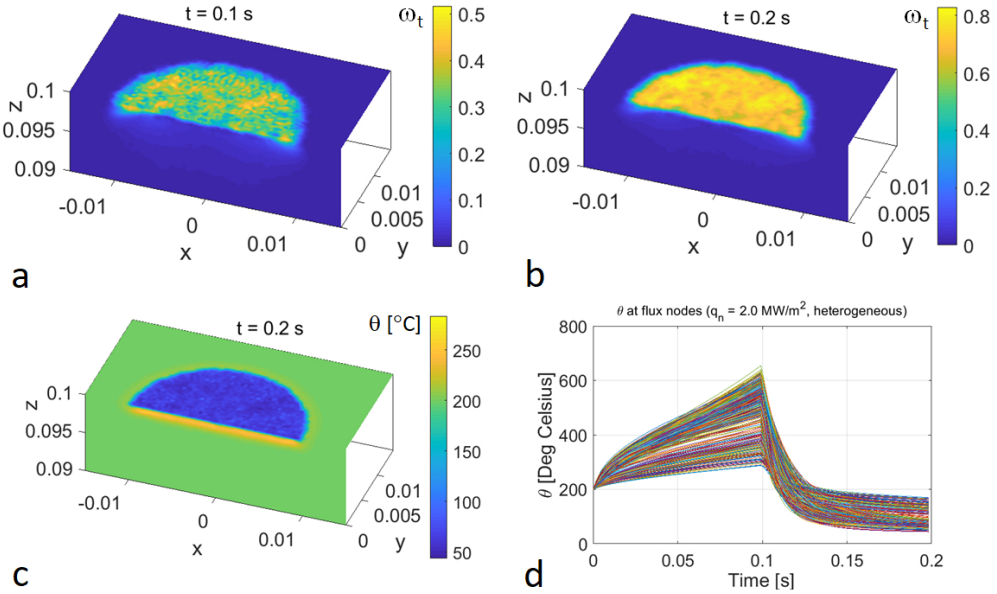

244x145mm (120 x 120 DPI)

Table 1. Material properties and model parameter values

Parameter/mineral	Quartz	Feldspars	Biotite	Homog
E [GPa]	80	60	20	63
σ_{t0} [MPa]	10	8	7	8
σ_{c0} [MPa]	180	180	180	180
ν	0.17	0.29	0.2	0.25
ρ [kg/m^3]	2630	2630	2800	2600
G_{Ic} [J/m^2]	40	40	28	39
G_{IIc} [J/m^2]	2000	2000	1400	1950
φ [°]	50	50	50	50
ψ [°]	5	5	5	5
s_{MR} [MPa·s]	0.25	0.25	0.25	0.25
s_{DP} [MPa·s]	0.3	0.3	0.3	0.3
A_t	0.98	0.98	0.98	0.98
A_c	0.98	0.98	0.98	0.98
α [1/K]	1.60E-5	0.75E-5	1.21E-5	1.067E-5
k [W/mK]	4.94	2.34	3.14	3.26
c [J/kgK]	731	730	770	733.5
f [%]	33	59	8	100